(Received 10 January 2025, Accepted 26 February 2025, Scheduled 17 March 2025)

Pattern Nulling for Advanced Linear Antenna Systems in 6G by Amplitude-Only Control via Deep Learning

Van Luyen Tong* and Huy Hoang Nguyen

Hanoi University of Industry, Hanoi 100000, Vietnam

ABSTRACT: This paper presents amplitude-only control beamforming approaches within advanced linear antenna systems (ALASs) for sixth generation (6G) technology. The principle of these approaches is training the radiation pattern alongside the weight set derived from two types of the linearly constrained minimum variance (LCMV) optimization problem, which are the single null (SN-LCMV) and broad null (BN-LCMV), using deep learning (DL). Thus, they are called SN-DL and BN-DL, respectively. The BN-DL effectively establishes the broad null, with the median magnitude at null being -37.44 dB. The computation time is notably reduced, attaining a speed that is 8.26 times faster than the BN-LCMV, 6.95 times faster than the SN-LCMV, and 1.11 times faster than the SN-DL. Over 1000 simulations, the BN-DL demonstrates the highest stability, achieving a peak density value of 10.17%, in comparison to the 3.09% recorded in SN-LCMV, 6.74% in BN-LCMV, and 6.94% in SN-DL, respectively.

1. INTRODUCTION

The fifth generation (5G) of cellular network technology debuted in mid-2019 in South Korea, and it has since grown to more than 1.5 billion subscribers, with a projected 2 billion by the end of 2025 [1]. However, it does not end there, and research organizations and scientists have been working to explore the 6G from the early deployment of 5G in certain key nations. Indeed, several surveys and technical studies focus on this cellular network technology [2–5]. There is a strong anticipation that 6G incorporating advanced techniques, such as the utilization of the terahertz frequency (THz) band for integrated sensing and communication (ISAC) [6, 7], the implementation of cloud access networks for cell-free massive multiple-input and multiple-output (MIMO) systems [8, 9], the deployment of reconfigurable intelligent surface (RIS) solutions [10, 11], and the integration of artificial intelligence (AI) [12, 13], will effectively supplant 5G by 2030 [1].

Beamforming is a spatial filtering technique extensively researched and utilized in several applications, including radar [14, 15], sonar [16, 17], medical [18, 19], speech processing [20, 21], and particularly in wireless communications from the third generation (3G) [22–24]. This technique is frequently employed in advanced antenna systems (AASs) installing at base stations or access points, to minimize noise and interference by nulling points in their direction via the control of amplitude, phase, and complex weights. Thus, the transmission/reception (TX/RX) qualities are enhanced whereas energy loss is reduced during operation, ultimately improving service quality and lowering installation and maintenance expenses. Commonly exploited beamforming algorithms that are low complex and effective involve LCMV [20], least mean squares (LMS) [21], minimum variance distortionless response (MVDR) [25], etc. Nowadays, when problems become complicated with more variables and exhibit non-convexity, the aforementioned algorithms become inefficient. Consequently, approximation optimization approaches such as alternating optimization (AO) [11] and semidefinite relaxation (SDR) [26], as well as nature-inspired metaheuristics including particle swarm optimization (PSO) [27], bat algorithm (BA) [28], and firefly algorithm (FA) [10] have emerged.

Numerous studies show that, although nature-inspired metaheuristics surpass traditional and approximation optimization approaches [10, 27, 28], their execution time is significantly greater than the submillisecond requirement for 6G [2–5]. As a result, the application of deep learning (DL), which is known as a real-time approach in object detection [29] and image segmentation [30], has arisen as a phenomenon to solve this problem in beamforming. This approach fundamentally involves using the features and weights derived from the optimization problem and technique, respectively, and subsequently training them via a CNN to acquire a set of deep weights. In 2019, Zhao et al. developed a CNN-based phase-only nulling linear beamformer that used the interference covariance matrix as input to the network [31]. The array antenna can establish nulls at undesirable locations, whereas preserving the original magnitude of the side lobes. This approach is notably popular and bears resemblance to the research conducted by Ramezanpour et al. in 2020 [32] and Liao et al. in 2023 [33], with complex weights. Another significant approach by Bianco et al. in 2020 is to use the radiation pattern derived from an optimization approach as the input for a CNN [34]. This solution is reported to be up to 1700 times faster than the original optimization problem on their device, whereas still fulfilling the constraints. The practical implementation of this approach is also challenging. Nonetheless, it is not unfeasible.

* Corresponding author: Van Luyen Tong (luyentv@haui.edu.vn).

Realizing the potential of research [34], this study presents an amplitude-only control beamforming approach in ALAS for 6G communication technology, dubbed BN-DL. It is based on training radiation patterns and weights derived from the BN-LCMV optimization problem via a CNN. The simulation results indicate that the BN-DL successfully locates the broad null at the interference location, achieving a speed that is 8.26 times faster than the BN-LCMV, despite having a greater magnitude. In comparison with the SN-LCMV problem and SN-DL, the BN-DL exhibits a magnitude at null lying between the SN-LCMV and SN-DL. Furthermore, the computation time of the proposed approach is 6.95 times more efficient than the SN-LCMV and 1.11 times than the SN-DL.

The subsequent sections of the paper are structured as follows. First, the problem formulation is presented in Section 2. Next, Section 3 details the LCMV optimization problems and DL-based beamforming algorithm. After that, Section 4 presents and discusses the simulation results, before concluding in Section 5.

Notation: a and A are the scalars, whereas $\mathbf{a}$ and $\mathbf{A}$ correspond a column vector and a matrix. The superscripts T and H represent the transpose and conjugate transpose of a matrix, respectively; $\triangleq$ denotes a definition; $\cup$ is a union; $\mathbb{C}$ and $\mathbb{R}$ are respectively the sets of complex and real numbers.

2. PROBLEM FORMULATION

Figure 1 shows an ALAS as a uniform linear array (ULA) with N elements positioned along the y-axis of the Cartesian coordinate system, with a spacing of $d = \lambda/2$, where λ denotes the wavelength of D THz-band radio signals. These signals come from the angle $\psi = [\phi, \theta]$ in which $\phi \in [-90°, 90°]$ from the azimuth plane (xy-plane), whereas $\theta \in [-90°, 90°]$ from the elevation plane (yz-plane). However, due to the beamforming weight vector $\mathbf{w} \triangleq [w_1, \ldots, w_N]^T \in \mathbb{R}^{N\times 1}$, we specify that the desired signal comes solely from $\psi_0 = [0°, 0°]$, but the interference remains as previously defined.

With $\mathbf{s}(n) \triangleq [s_0(n), \ldots, s_{D-1}(n)]^T \in \mathbb{R}^{D\times 1}$ being the incoming signal at time n and $\mathbf{V}_s(\psi) \triangleq [\mathbf{v}(\psi_0), \ldots, \mathbf{v}(\psi_{D-1})] \in \mathbb{C}^{N\times D}$ being the steering vector matrix of the array, the output

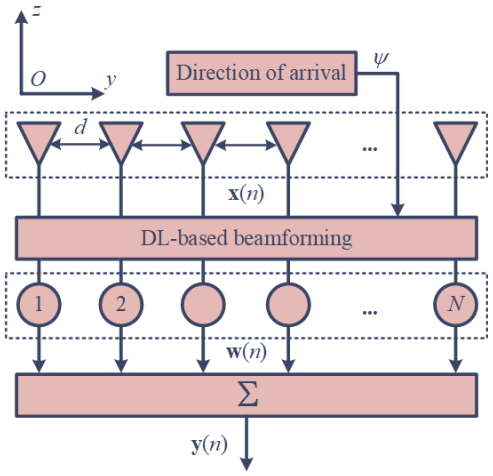

FIGURE 1. Block diagram of a N-element ALAS.

of the array at time n is written as follows:

$$\begin{aligned}\mathbf{y}(n) &= \mathbf{w}(n)^H \mathbf{x}(n) \\ &= \mathbf{w}(n)^H \mathbf{v}(\psi_0) s_0(n) + \sum_{i=1}^{D-1} \mathbf{w}(n)^H \mathbf{v}(\psi_i) s_i(n) + \epsilon(n), \end{aligned} \quad (1)$$

where $\mathbf{x}(n) \triangleq [x_1(n), \ldots, x_N(n)]^T \in \mathbb{C}^{N\times 1}$ is the total signal at the array at the time n; $\mathbf{v}(\psi_0)$, s_0, and $\mathbf{v}(\psi_i)$, s_i, $i = 1, \ldots, D-1$, correspondingly, are the steering vector and the signal of the target one and interferences; and $\epsilon \in \mathbb{R}$ is the environmental noise. Each vector $\mathbf{v}(\psi_i)$ can be represented in detail as follows:

$$\mathbf{v}(\psi_i) = [1, e^{j\beta d \sin(\phi_i)\sin(\theta_i)}, \ldots, e^{j\beta(N-1)d\sin(\phi_i)\sin(\theta_i)}]^T, \quad (2)$$

where j and $\beta = \frac{2\pi}{\lambda}$ are the imaginary component and the wave number of the incoming signal. The interference inflicted at the desired signal is expressed as follows:

$$I = \sum_{i=1}^{D-1} |\mathbf{w}^H \mathbf{v}(\psi_i)|^2 = \sum_{i=1}^{D-1} \mathbf{w}^H \mathbf{v}(\psi_i)\mathbf{v}(\psi_i)^H \mathbf{w}. \quad (3)$$

3. PROPOSED APPROACH

3.1. LCMV Optimization Problem

Based on the problem description in Section 2, we establish a single null LCMV optimization problem as follows:

$$\begin{aligned} \min_{\mathbf{w}} \quad & \sum_{i=1}^{D-1} \mathbf{w}^H \mathbf{v}(\psi_i)\mathbf{v}(\psi_i)^H \mathbf{w} \\ \text{s. t.} \quad & \mathbf{w}^H \mathbf{v}(\psi_0) = 1, \\ & \mathbf{w}^H \mathbf{v}(\psi_i) = 0,\ i = 1, \ldots, D-1. \end{aligned} \quad (4)$$

To reduce errors resulting from rapid shifts in the direction of arrival or inaccuracies of the estimation, a broad null technique is employed by applying P nulls positioned around each original interference. Then, problem (4) becomes the broad null LCMV as follows:

$$\begin{aligned} \min_{\mathbf{w}} \quad & \sum_{i=1}^{D-1} \sum_{p=1}^{P} \mathbf{w}^H \mathbf{v}(\psi_{i,p})\mathbf{v}(\psi_{i,p})^H \mathbf{w} \\ \text{s. t.} \quad & \mathbf{w}^H \mathbf{v}(\psi_0) = 1, \\ & \mathbf{w}^H \mathbf{v}(\psi_{i,p}) = 0,\ i = 1, \ldots, D-1, \\ & p = 1, \ldots, P. \end{aligned} \quad (5)$$

The drawback of possessing a wide null with significant depth is that the side lobe level may rise substantially, and this cannot be regulated. This is a significant trade-off, and nevertheless, this work concentrates on mitigating the interference instead of attempting to control the side lobe level.

3.2. Proposed DL-Based Algorithm

Upon acquiring the real weights from the LCMV problems, we compute the radiation pattern in decibel (dB) with the resolution of 1° as follows:

$$P_R = 20\log\left(|\mathbf{w}^H\mathbf{v}(\psi)|\right). \quad (6)$$

Because of the limit of the elevation and azimuth plane, P_R is characterized by a dimension of 181×181. This study focuses on a 64-element ALAS. The amplitude controller is fundamentally designed with a zero imaginary component. However, after the training data are normalized via z-score, this imaginary component changes into a non-zero constant. As a result, the output of the CNN, which incorporates the 64 real weights, consists of a normalized phase value and is structured as 1×65.

The architecture of the 24-layer CNN is illustrated in Fig. 2, where, as previously stated, the input is a (181×181)-matrix, and the output is a 65-element row vector. The CNN comprises 1.8×10^6 learnable parameters, with data processed through 5 encoding stages and 3 decoding stages. Each encoding stage consists of a convolutional layer (Conv), supplemented by a batch normalization layer (BNm) and a modified leaky rectified linear unit (LReLU) with the amplification factor of 0.1. The first encoding stage employs a (1×16)-filter; the subsequent layer escalates to 16×32; and the final three stages maintain a size of 32×32. In the decoding stages, a fully connected (FC) layer is employed in conjunction with a BNm and an LReLU as the encoder. The first two FC layers have a length of 512, whereas the last FC layer has a length of 65, corresponding to 64 weights which range from 1 to N and the phase value. Finally, the predicted data are assessed at the regression layer using mean square error (MSE) or l_2 norm.

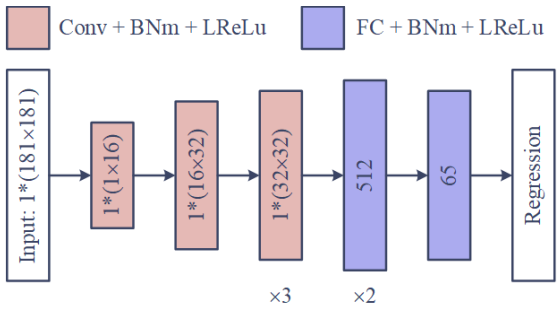

FIGURE 2. The architecture of the proposed CNN.

In the case of the SN-LCMV with an even N, the outcome is a symmetric set of weights. Therefore, the CNN constructed for this problem differ only from the CNN designed for the BN-LCMV in the final FC layer, which has a length of 33, representing 32 weights varying from 1 to $N/2$ and the phase value.

We generate 2×10^5 data for the dataset of each case, allocating 80% for training and 20% for validation, detailed as follows. The main beam is anchored at ψ_0, whereas an interference is randomly produced following the uniform distribution (UD), from -90° to 90°. However, the interference lies outside the first null beamwidth (FNBW) in the azimuth plane of the radiation pattern, which is computed by the following formula:

$$\text{FNBW} = \frac{2}{Nd/\lambda} = \frac{2}{64 \times 0.5} = 62.5 \times 10^{-3} \text{ rad}, \quad (7)$$

approximately with 3.58°, i.e., the interference can come from $\psi_1 \in [-90^\circ, -1.79^\circ] \cup [1.79^\circ, 90^\circ]$. We establish $P = 25$, i.e., the broad null is squared with the side length of 3°. Furthermore, the level of the interference is also created following the UD from -20 dB to -50 dB.

Regarding the training options, we train and test on a workstation computer Intel(R) Xeon(R) Bronze 3104 CPU @1.70 GHz, 48 GB RAM and three NVIDIA Quadro P2200 GPUs. The mini-batch size is set to 32. The learnable parameters is updated by the default adaptive moment (ADAM) estimation optimizer. The initial learning rate is 10^{-3}, which is reduced by 0.1 every 6 epochs throughout 30 epochs. The data are shuffled for every epoch.

4. SIMULATION AND DISCUSSION

In this section, we present the results, compare and discuss the SN-LCMV (4), SN-DL, BN-LCMV (5), and BN-DL approaches. Firstly, Fig. 3 illustrates the training results of SN-DL and BN-DL in terms of loss and root mean square error (RMSE). It is clear that BN-DL converges more rapidly than SN-DL, achieving convergence at the 8-th epoch with BN-Loss and BN-RMSE values of 0.65 and 1.14, respectively. Conversely, although the SN-DL converges later at the 13-th epoch, it demonstrates significantly improved SN-RMSE and SN-Loss values of 0.12 and 0.0067, respectively. This betterment can be attributed to the fact that the output size of SN-DL is nearly half that of BN-DL.

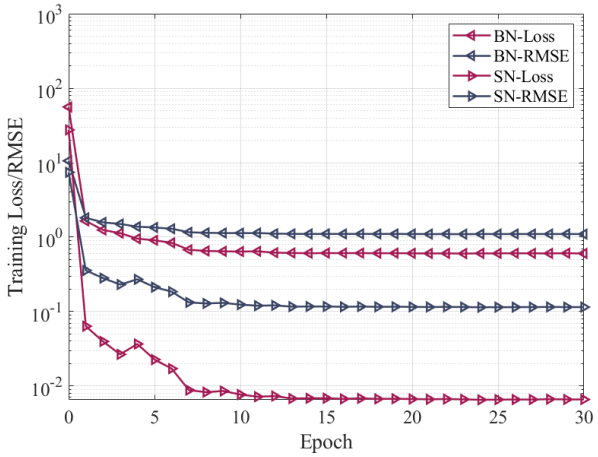

FIGURE 3. The training results versus epochs.

Next, we demonstrate the radiation patterns generated by the approaches for the scenario where $\psi_1 = [-30^\circ, -30^\circ]$ over 50 times. Fig. 4 shows that both the BN-DL and SN-DL effectively replicate radiation patterns that closely resemble those of the BN-LCMV and SN-LCMV, respectively. However, a distinction is observed in the null location. The null magnitudes of the BN-LCMV and SN-LCMV are less than those represented

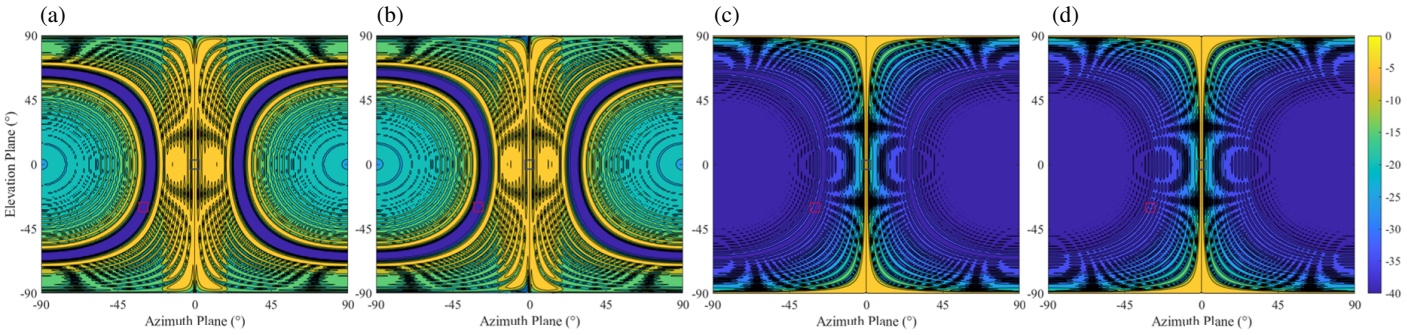

FIGURE 4. The 3D radiation pattern in the case of $\psi_1 = [-30°, -30°]$ of (a) the BN-LCMV, (b) the BN-DL, (c) the SN-LCMV and (d) the SN-DL.

in the color map, resulting in the visibility of only a dark blue region, indicating levels below -35 dB. For BN-DL and SN-DL, it is obvious that null points are located at undesired angles ψ_1, which can be attributed to training errors and approximations made during the data normalization process. The side lobes produced by the single null problem exhibit significantly better control than the broad null problem. This is evidenced by the greater magnitude of the side lobes in the broad null, particularly at angles close to the main lobe.

The radiation patterns presented in the cutting plane are illustrated in Fig. 5. At the cutting plane at $\theta = 0°$, the main beamwidth for both the BN and SN cases measures $4°$. However, the side lobe levels in the SN case have an immediate decrease thereafter, whereas the BN case only begins to show a reduction after going through the broad null. It can also be seen that the distinction between LCMV and DL appears minimal. At the cutting plane at $\theta = -30°$, the precise null point of BN-LCMV remains elusive due to the wide and deep null region. In contrast, SN-LCMV accurately positions the null point at -46.95 dB. Similarly, both SN-DL and BN-DL establish their null points at -35.64 dB and -37.91 dB, respectively. Upon closer look, it becomes evident that the broad null of BN-DL consists of four null points, resulting in a null region that covers $13°$ starting at the -3 dB point. At the cutting plane at $\phi = -30°$, while all three approaches correctly position the null point at the interference, the SN-DL results in the null being placed wrongly.

In order to evaluate the execution speed of the proposed approach, we conducted measurements of the average time required to compute the weights over 100 times. We execute the LCMV problems using the CVX optimizer [35] developed by Grant and Boyd, and the results are given in Table 1. Firstly, the computation time of BN-LCMV is longer than SN-LCMV, primarily attributable to the time required for generating pseudo nulls. The computation time of BN-DL, when being assessed using either CPU or GPU, is less than SN-DL, mainly due to

TABLE 1. The average time to compute weights.

BN-LCMV (CPU)	BN-DL (CPU)	BN-DL (GPU)
402.65 ms	62.35 ms	48.765 ms
SN-LCMV (CPU)	SN-DL (CPU)	SN-DL (GPU)
339.11 ms	74.311 ms	54.248 ms

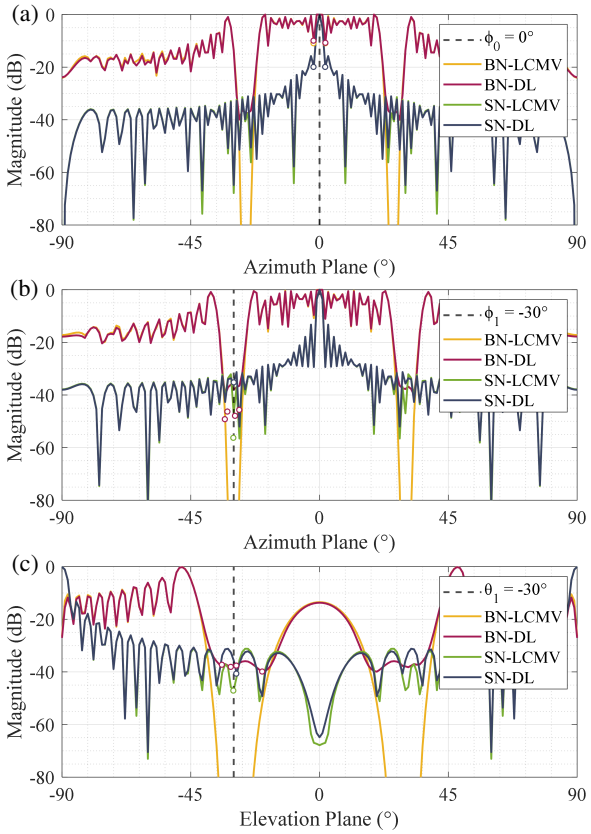

FIGURE 5. The radiation pattern in the case of $\psi_1 = [-30°, -30°]$ in azimuth plane cut at (a) $\theta = 0°$, (b) $\theta = -30°$ and in elevation plane cut at (c) $\phi = -30°$.

the weight regeneration step. In the case of SN-DL, it replicates the weights from $N/2 + 1$ to N applying the training weights from 1 to $N/2$. This particular step is the most time-consuming. From there, it can be determined that BN-DL exhibits a computation speed that surpasses BN-LCMV by 8.26 times, exceeds SN-LCMV by 6.95 times, and is approximate to SN-DL, being 1.11 times faster. Although the simulation times on our PC do not fulfill the latency requirement for 6G, specialized devices and controllers are capable of achieving these benchmarks in practical applications.

In relation to the stability of the approaches, we performed over 1000 simulations to evaluate them, and the resulting magnitude distribution of null is illustrated in the violin plot pre-

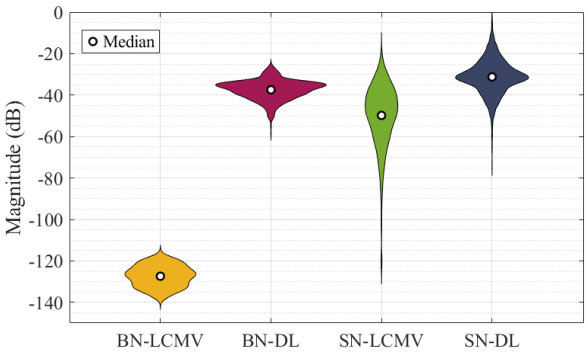

FIGURE 6. The distribution of the null's magnitude.

sented in Fig. 6. In comparison to the other three approaches, BN-LCMV demonstrates superior reliability, as evidenced by its concentration within the range of -140 dB to -115 dB. The median value is recorded at -127.39 dB, whereas the peak density value reaches 6.74% at -126.4 dB. This stands in contrast to the SN-LCMV, and this approach can approximate the value with BN-LCMV but may also yield values around -20 dB. The median is -48.81 dB, with the peak density value at -45.32 dB being 3.09%. Approaches employing DL demonstrate significantly higher peak density values than traditional approaches. Concerning the BN-DL, the values vary from -55 dB to -25 dB, with a median of -37.44 dB, and the highest peak density value is recorded at -35 dB, representing 10.17%. Meanwhile, the SN-DL, whereas exhibiting a median nearly equivalent to that of the DN-DL at -31.23 dB, tends to yield values predominantly around -10 dB, which is significantly elevated in comparison to the other approaches. The peak density value obtained from this approach is -31.32 dB, which corresponds to 6.94% and approximates to BN-LCMV.

5. CONCLUSION

The approach presented in this paper shows effectiveness with a fixed target angle and is influenced by interference, resulting in a response time that significantly surpasses traditional optimization problems. This approach is also useful in applications related to the Internet of Things (IoT), where the implementation of a real-time beamforming technique is crucial for enhancing user experience. In pursuit of practical application, future studies will incorporate the generation of a real antenna radiation pattern as input for better outcomes.

REFERENCES

[1] Jiang, W. and B. Han, *Cellular Communication Networks and Standards: The Evolution from 1G to 6G*, Springer Nature Switzerland, 2024.

[2] Yang, P., Y. Xiao, M. Xiao, and S. Li, "6G wireless communications: Vision and potential techniques," *IEEE Network*, Vol. 33, No. 4, 70–75, 2019.

[3] Alsabah, M., M. A. Naser, B. M. Mahmmod, S. H. Abdulhussain, M. R. Eissa, A. Al-Baidhani, N. K. Noordin, S. M. Sait, K. A. Al-Utaibi, and F. Hashim, "6G wireless communications networks: A comprehensive survey," *IEEE Access*, Vol. 9, 148 191–148 243, 2021.

[4] Zhao, Y., W. Zhai, J. Zhao, T. Zhang, S. Sun, D. Niyato, and K.-Y. Lam, "A comprehensive survey of 6G wireless communications," *ArXiv Preprint ArXiv:2101.03889*, 2021.

[5] Mohsan, S. A. H. and Y. Li, "A contemporary survey on 6G wireless networks: Potentials, recent advances, technical challenges and future trends," *ArXiv Preprint ArXiv:2306.08265*, 2023.

[6] Lyu, J., Q. Liu, and G. Wang, "Compressed sensing-based terahertz imaging algorithm in 6G-ISAC terminal systems," in *2024 Joint European Conference on Networks and Communications & 6G Summit (EuCNC/6G Summit)*, 398–403, Antwerp, Belgium, Jun. 2024.

[7] Taghavi, E. M., H. Saarnisaari, and M. Juntti, "Fundamental and practical performance assessment in monostatic ISAC: From sub-6 GHz to sub-THz," in *2024 3rd International Conference on 6G Networking (6GNet)*, 221–226, Paris, France, Oct. 2024.

[8] Wang, Y. and D. Hu, "A left-null-space-based massive access method for cell-free massive MIMO systems," in *2023 5th International Conference on Computer Communication and the Internet (ICCCI)*, 168–173, Fujisawa, Japan, Jun. 2023.

[9] Femenias, G. and F. Riera-Palou, "From cellular to cell-free massive MIMO: A progressive approach towards 6G," in *2024 IEEE 25th International Workshop on Signal Processing Advances in Wireless Communications (SPAWC)*, 136–140, Lucca, Italy, Sep. 2024.

[10] Le, T. A. and X.-S. Yang, "Firefly algorithm for beamforming design in RIS-aided communication systems," in *2023 IEEE 97th Vehicular Technology Conference (VTC2023-Spring)*, 1–5, Florence, Italy, Jun. 2023.

[11] Le, T. A., D. W. K. Ng, and X.-S. Yang, "A rank-one optimization framework and its applications to transmit beamforming," *IEEE Transactions on Vehicular Technology*, Vol. 73, No. 1, 620–636, 2024.

[12] Thuc, K.-X., H. M. Kha, N. V. Cuong, and T. V. Luyen, "A metaheuristics-based hyperparameter optimization approach to beamforming design," *IEEE Access*, Vol. 11, 52 250–52 259, 2023.

[13] Nguyen, T.-H., H. Park, K. Seol, S. So, and L. Park, "Applications of deep learning and deep reinforcement learning in 6G networks," in *2023 Fourteenth International Conference on Ubiquitous and Future Networks (ICUFN)*, 427–432, Paris, France, Jul. 2023.

[14] Krieger, G., N. Gebert, M. Younis, and A. Moreira, "Advanced synthetic aperture radar based on digital beamforming and waveform diversity," in *2008 IEEE Radar Conference*, 1–6, Rome, Italy, May 2008.

[15] Chahrour, H., S. Rajan, R. Dansereau, and B. Balaji, "Hybrid beamforming for interference mitigation in MIMO radar," in *2018 IEEE Radar Conference (RadarConf18)*, 1005–1009, Oklahoma City, OK, USA, Apr. 2018.

[16] Somasundaram, S. D. and N. H. Parsons, "Evaluation of robust capon beamforming for passive sonar," *IEEE Journal of Oceanic Engineering*, Vol. 36, No. 4, 686–695, 2011.

[17] Somasundaram, S. D., "Wideband robust capon beamforming for passive sonar," *IEEE Journal of Oceanic Engineering*, Vol. 38, No. 2, 308–322, 2013.

[18] Matrone, G., A. S. Savoia, G. Caliano, and G. Magenes, "The delay multiply and sum beamforming algorithm in ultrasound B-mode medical imaging," *IEEE Transactions on Medical Imaging*, Vol. 34, No. 4, 940–949, 2015.

[19] Chen, J., J. Chen, H. Min, and X. Wang, "Real-time embedded implementation of adaptive beamforming for medical ultrasound imaging," in *2016 Sixth International Conference on Instrumentation & Measurement, Computer, Communication and Control*

(IMCCC), 356–360, Harbin, China, Jul. 2016.

[20] Habets, E. A. P., J. Benesty, S. Gannot, P. A. Naylor, and I. Cohen, "On the application of the LCMV beamformer to speech enhancement," in *2009 IEEE Workshop on Applications of Signal Processing to Audio and Acoustics*, 141–144, New Paltz, NY, USA, Oct. 2009.

[21] Nguyen, H. H., X. T. Pham, V. S. Doan, and M. K. Hoang, "Combining MUSIC algorithm and adaptive beamforming to improve online call quality," in *International Conference on Ad Hoc Networks*, 3–14, 2023.

[22] Chen, Y., J. Speidel, C. Hoek, and S. Russ, "Investigation of diversity and beamforming techniques for UMTS high speed downlink packet access," in *2005 IEEE 16th International Symposium on Personal, Indoor and Mobile Radio Communications*, Vol. 4, 2332–2336, Berlin, Germany, Sep. 2005.

[23] Awan, A. A., Irfanullah, S. Khattak, and A. N. Malik, "Performance comparisons of fixed and adaptive beamforming techniques for 4G smart antennas," in *2017 International Conference on Communication, Computing and Digital Systems (C-CODE)*, 17–20, Islamabad, Pakistan, March 2017.

[24] Matalatala, M., M. Deruyck, E. Tanghe, L. Martens, and W. Joseph, "Simulations of beamforming performance and energy efficiency for 5G mm-wave cellular networks," in *2018 IEEE Wireless Communications and Networking Conference (WCNC)*, 1–6, Barcelona, Spain, Apr. 2018.

[25] Tuladhar, S. R. and J. R. Buck, "Unit circle MVDR beamformer," in *2015 IEEE International Conference on Acoustics, Speech and Signal Processing (ICASSP)*, 2484–2488, South Brisbane, QLD, Australia, Apr. 2015.

[26] Le, T. A., H. X. Nguyen, Q.-T. Vien, and M. Karamanoglu, "Secure information transmission and power transfer in cellular networks," *IEEE Communications Letters*, Vol. 19, No. 9, 1532–1535, 2015.

[27] Souto, V. D. P., R. D. Souza, B. F. Uchôa-Filho, A. Li, and Y. Li, "Beamforming optimization for intelligent reflecting surfaces without CSI," *IEEE Wireless Communications Letters*, Vol. 9, No. 9, 1476–1480, 2020.

[28] Van Luyen, T. and T. V. B. Giang, "Null-steering beamformer using bat algorithm," *Applied Computational Electromagnetics Society Journal (ACES)*, Vol. 33, No. 1, 23–29, 2018.

[29] Karatas, G., O. Demir, and O. K. Sahingoz, "Deep learning in intrusion detection systems," in *2018 International Congress on Big Data, Deep Learning and Fighting Cyber Terrorism (IBIGDELFT)*, 113–116, Ankara, Turkey, Dec. 2018.

[30] Liu, G. and Y. Zhao, "A survey of deep learning methods for MRI brain tumor image segmentation," in *2022 4th International Conference on Machine Learning, Big Data and Business Intelligence (MLBDBI)*, 318–323, Shanghai, China, Oct. 2022.

[31] Zhao, Z., H. Zhao, M. Zheng, and J. Tang, "Real-time phase-only nulling based on deep neural network with robustness," *IEEE Access*, Vol. 7, 142 287–142 294, 2019.

[32] Ramezanpour, P., M. J. Rezaei, and M. R. Mosavi, "Deep-learning-based beamforming for rejecting interferences," *IET Signal Processing*, Vol. 14, No. 7, 467–473, 2020.

[33] Liao, Z., K. Duan, J. He, Z. Qiu, and B. Li, "Robust adaptive beamforming based on a convolutional neural network," *Electronics*, Vol. 12, No. 12, 2751, 2023.

[34] Bianco, S., P. Napoletano, A. Raimondi, M. Feo, G. Petraglia, and P. Vinetti, "AESA adaptive beamforming using deep learning," in *2020 IEEE Radar Conference (RadarConf20)*, 1–6, Florence, Italy, Sep. 2020.

[35] Grant, M. and S. Boyd, "CVX: Matlab software for disciplined convex programming, version 2.1," https://cvxr.com/cvx, Mar. 2014.